An Accurate Magnetic Equivalent Circuit Model for Modeling and Analysis of Variable Reluctance Energy Harvesters

Farhad Rezaee-Alam*

Departement of Electrical Engineering, Lorestan University, 68151-44316, Khorramabad, Lorestan, Iran, +989166591727, Rezaee.fa@lu.ac.ir, farhad.rezaee.alam@gmail.com

Abstract

Variable reluctance energy harvester (VREH) is a good candidate of transducers to transform the environmental energy into electricity. VREHs act based on electromagnetic induction due to the variation of air-gap reluctance with the rotation of wheel. This paper presents an accurate analytical model based on magnetic equivalent circuit (MEC) model and conformal mappings (CMs) for electromagnetic modeling the VREHs, which have a large air-gap. The geometry of analyzed VREH on both sides of air-gap including the iron parts, slots, and permanent magnets (PMs) is divided into many elements in cylindrical coordinate, and each element is then replaced with an equivalent permeance model. The air-gap region is modeled with permeances calculated by the CM method, which can accurately consider the real paths of flux tubes in large air-gap. The obtained air-gap permeances are then used in MEC model for electromagnetic modeling and analysis of studied VREH, while considering the effects of slots and magnetic saturation, accurately. In final, the analytical results are verified by comparing with the corresponding results obtained through finite element method (FEM).

Index Terms: air-gap; conformal mapping (CM); magnetic equivalent circuit (MEC); permanent magnet (PM); permeance; variable reluctance energy harvester (VREH).

1. Introduction

Energy harvesting technology provides a sustainable energy source for supplying the low power electronic devices in industrial applications by using the environmental energies such as thermal energy [1], kinetic energy [2], solar energy [3], and wind energy [4]. Energy harvesters (EHs) usually act based on electromagnetic method [5]-[6], or electrostatic method [7], or other techniques for harvesting the energy from environment. The rotational motion is one of the main forms of kinetic energy, which is accessible through engine, wind turbine, and so on. For this reason, EHs with electromagnetic structures have been attracted plenty of attentions [8]-[9]. However, many EHs cannot accurately act under low rotation speed. To overcome this problem,

different structures of EH have been proposed for low frequency rotation such as circular halbach electromagnetic EH [10]-[11], and variable reluctance energy harvester (VREH) [9]. The main work of both electromagnetic structures is to generate an induced voltage based on Faraday's law of induction.

Figure 1

Unlike the traditional electromagnetic EHs, the position of permanent magnets (PMs) and pick-up coils in VREHs is stationary. As shown in Figure 1, one typical VREH has a toothed wheel, one m-shaped pole-piece including two PMs, and one pick-up coil. VREHs have been used in different applications such as railroad surveillance system [12], and wireless wheel speed sensor [13]. With the rotation of toothed wheel, the magnetic flux due to PMs will be varying as the air-gap reluctance changes. Therefore, it is necessary to predict the induced voltage in pick-up coil, accurately. In [9], an analytic technique based on substituting angle-magnetic field division (SA-MFD) was proposed to calculate the air-gap permeance of VREHs. However, SA-MFD method is a cumbersome technique, and it is not user-friendly and accurate method. In [14], finite element method (FEM) was used to analyze the six structures of VREHs. However, FEM is a time-consuming technique, and it is better to be used in final stage for verifying the analytical results. As we know, VREHs are placed in the category of large air-gap electromagnetic devices. For this reason, an accurate magnetic equivalent circuit (MEC) model is presented in this paper, which can consider the real paths of flux tubes in large air-gap. Main parameters of analyzed VREH are introduced in Table. 1. This paper is organized as follows:

MEC model will be introduced in section 2 for modeling the studied VREH. The results obtained through MEC model are presented and analyzed in section 3. The conclusions of work are also presented in section 4.

Table 1

2. MEC model of analyzed VREH

MEC model is a famous technique for modeling and analysis of all electromagnetic devices [15]-[17]. A simple MEC model was used in [15] to design and model a novel electromagnetic EH. The proposed MEC model in this paper acts based on dividing the geometry of VREH (except for air-gap) into many elements in cylindrical coordinate.

2.1. MEC model of non-air-gap region

Figure 2 shows the MEC model of analyzed VREH. The equivalent permeance network for each element in outside the air-gap region is shown in Figure 2b while considering the radial and tangential paths for flux tubes. The reason for choosing this element type is defining the geometry of analyzed VREH in cylindrical coordinate system. To calculate the radial and tangential permeance (G_r and G_t) for each element (as shown in Figure 2b), consider one differential element with radial length *dr* and angular width dα at the position of *(r,α)*, as shown in Figure 3.

Figure 2

Figure 3

For one typical differential element shown in Figure 3, $dG_R\,(r,\alpha)$ and $dG_T\,(r,\alpha)$ can be defined as follows:

$$\begin{cases} dG_R\left(r,\alpha\right) = \dfrac{\mu_0 \times \mu_{r,r} \times r \times d\alpha \times L}{dr} \\ dG_T\left(r,\alpha\right) = \dfrac{\mu_0 \times \mu_{r,t} \times dr \times L}{r \times d\alpha} \end{cases} \tag{1}$$

where μ_0 is the magnetic permeability of air, L is the axial length of analyzed VREH, $\mu_{r,r}$ and $\mu_{r,t}$ are respectively the radial and tangential components of the relative magnetic permeability (μ_r) of relevant differential element.

All differential elements $dG_R(r,\alpha)$ at radius of "r" are in parallel magnetic connection. All differential elements $dG_T(r,\alpha)$ at the angle of "α" are also in parallel magnetic connection. Therefore, for one typical element as shown in Figure 2b, total radial permeance (G_R) and total tangential permeance (G_T) can be calculated as follows:

$$dG_R\left(r\right) = \int_0^{\beta} dG_R\left(r,\alpha\right) \;\rightarrow\; dG_R\left(r\right) = \frac{\mu_0 \times \mu_{r,r} \times r \times \beta \times L}{dr} \rightarrow$$

$$\frac{1}{G_R} = \int_{r_1}^{r_2} \frac{1}{dG_R\left(r\right)} \;\rightarrow\; G_R = \frac{\mu_0 \times \mu_{r,r} \times \beta \times L}{ln\left(\dfrac{r_2}{r_1}\right)} \tag{2}$$

$$dG_T(\alpha)=\int_{r_1}^{r_2} dG_T(r,\alpha) \rightarrow dG_T(\alpha)=\frac{\mu_0\times\mu_{r,t}\times L\times ln\left(\frac{r_2}{r_1}\right)}{d\alpha} \rightarrow$$

$$\frac{1}{G_T}=\int_0^{\beta}\frac{1}{dG_T(\alpha)} \rightarrow G_T=\frac{\mu_0\times\mu_{r,t}\times L\times ln\left(\frac{r_2}{r_1}\right)}{\beta} \quad (3)$$

According to Figure 2b, total radial and tangential permeances (G_R and G_T) are separately shown with two series permeances G_r and G_t. Therefore, G_r and G_t are calculated as follows:

$$G_r=\frac{2\times\mu_0\times\mu_{r,r}\times\beta\times L}{ln\left(\frac{r_2}{r_1}\right)}$$

$$G_t=\frac{2\times\mu_0\times\mu_{r,t}\times L\times ln\left(\frac{r_2}{r_1}\right)}{\beta} \quad (4)$$

where, $\mu_{r,r}$ and $\mu_{r,t}$ can be calculated for relevant non-linear branch in MEC model as follows:

$$\begin{cases} H_t=\frac{\left|U(i,j)-U(i,j+1)\right|}{dl_t} \rightarrow B_t=f(H_t) \rightarrow \mu_{r,t}=12000\times e^{-0.8\times B_t{}^2} \\ H_r=\frac{\left|U(i,j)-U(i+1,j)\right|}{dl_r} \rightarrow B_r=f(H_r) \rightarrow \mu_{r,r}=12000\times e^{-0.8\times B_r{}^2} \end{cases} \quad (5)$$

where U is the matrix of scalar magnetic potential. H_t and B_t are respectively the tangential components of magnetic field intensity and magnetic flux density. H_r and B_r are respectively the radial components of magnetic field intensity and magnetic flux density. Figure 4 shows the B-H curve of material used in wheel and m-shaped pole.

Figure 4

Figure 5 **Figure 6**

PMs used in studied VREH are radial magnetized. Each element of PMs is replaced with equivalent line currents as shown in Figure 5. These equivalent line currents are calculated as follows:

$$\vec{M} = \frac{B_r}{\mu_0}\vec{a_r}$$
$$\vec{J_s} = \vec{M} \times \vec{a_n} \qquad (6)$$
$$I_m = \left|\vec{J_s}\right| \times dl$$

where B_r is remanent flux density of PM, $\overrightarrow{a_n}$ is generally the unit vector perpendicular to the relevant surface, $\overrightarrow{a_r}$ is the unit vector in radial direction, $\vec{M}$ is the magnetization vector, $\vec{J_s}$ is the vector of surface current density, dl is the length of relevant side, I_m and $-I_m$ are the magnitude of equivalent line currents.

As shown in Figure 5, an equivalent virtual coil with one turn can be considered for each PM element, which its MMF is as follows:

$$F = I_m \qquad (7)$$

Figure 6 shows the equivalent circuit for each PM element with radial magnetization. The equivalent circuit of other elements which place in air is similar to Figure 2 while considering $\mu_{r,r} = 1$ and $\mu_{r,t} = 1$.

Figure 7

2.2. MEC model of air-gap region

The main defect of MEC model is in the modeling of air-gap region. In [9] and [18-20], the air-gap permeances were calculated based on considering the radial and circular flux tubes in air-gap and slot region, respectively. However, the proposed technique in [9] and [18-20] is cumbersome and not user-friendly. Ostovic presented an analytic formula for calculating the mutual air-gap permeances [21], which has been used in many references [22-24] as follows:

$$G_{i,j}(\theta_r) = \begin{cases} G_{max} & 0 \le \theta_r \le \theta_2 \ \text{and} \ (2\pi - \theta_2) \le \theta_r \le 2\pi \\ \frac{G_{max}}{2} \times \left(1 + cos\left(\frac{\pi(\theta_r - \theta_2)}{\theta_1 - \theta_2}\right)\right) & \theta_2 \le \theta_r \le \theta_1 \\ \frac{G_{max}}{2} \times \left(1 + cos\left(\frac{\pi(\theta_r - 2\pi + \theta_2)}{\theta_1 - \theta_2}\right)\right) & (2\pi - \theta_1) \le \theta_r \le (2\pi - \theta_2) \\ 0 & \theta_1 \le \theta_r \le (2\pi - \theta_1) \end{cases} \qquad (8)$$

Where θ_r is the position of moving part, $\theta_1 = \frac{|W_i+W_j|}{D_g}$, $\theta_2 = \frac{|W_i-W_j|}{D_g}$, W_i and W_j are respectively the angular width of elements on both sides of air-gap, and D_g is the average diameter of air-gap. However, the proposed technique by Ostovic cannot consider the fringing and concentration of air-gap flux tubes. To remove these drawbacks, the cylindrical and pentagonal meshes have been used in air-gap region which lead to high computational load [16-17].

This paper presents a new technique based on conformal mappings (CMs) for calculating the mutual air-gap permeances, which can consider the real paths of air-gap flux tubes without high computational load. Figure 7a-b shows a zoomed view of analyzed VREH for illustrating the permeance between ith element of m-shaped pole-piece and jth element of the wheel. To calculate $G_{i,j}(\theta_r)$, Figure 7c shows a zoomed view of an annular domain which is including two virtual coils on both ends of relevant element, respectively. Ideal iron is considered for m-shaped pole-piece and wheel to calculate $G_{i,j}(\theta_r)$. The mutual air-gap permeance $G_{i,j}(\theta_r)$ is then calculated as follows:

$$G_{i,j}(\theta_r) = \left.\frac{\lambda_j(\theta_r)}{I_i}\right|_{I_j = 0} \tag{9}$$

where $\lambda_j(\theta_r)$ is the flux-linkage with jth virtual coil due to the excitation of ith virtual coil with $I_i(A)$. $\lambda_j(\theta_r)$ can be calculated as follows:

$$\lambda_j(\theta_r) = R_g \times L \times \int_0^{2\pi} \left[n_j(\alpha,\theta_r) \times B_r(\alpha,\theta_r) \right] d\alpha \tag{10}$$

where R_g is the radius of contour inside the air-gap, L is the axial length of analyzed VREH, α is the circumferential position of typical points on the contour in the air-gap, θ_r is the position of wheel, $n_j(\alpha,\theta_r)$ is the turn-function [25] of j^{th} virtual turn function, and $B_r(\alpha,\theta_r)$ is the distribution of radial component of air-gap flux density in the air-gap.

Figure 8

In proposed approach, the CM method [22] is used to calculate $B_r(\alpha,\theta_r)$ due to $I_i(A)$. To this end, as shown in Figure 8, one CM is used to transform the physical annular domain into the canonical annular domain in ψ-plane. This CM is used for having an annular domain with average radius of one meter in ψ-plane $(b < 1 < a)$. Hague's solution [26-27] is then used to calculate the scalar magnetic potential at typical points on the contour in the air-gap as follows:

$$\Omega(r,\alpha)=\sum_{k=1}^{2}\sum_{n=1}^{\infty}\left(\left[A_{n,k}-\frac{I_k}{2n\pi a^n}\right]r^n+B_{n,k}r^{-n}\right)sin\left(n\times\Delta\alpha_k\right)$$

$$A_{n,k}=\frac{-I_k\left(\mu_1-\mu_2\right)\left[b^{2n}\left(\mu_3-\mu_2\right)+a^{2n}\left(\mu_3+\mu_2\right)\right]}{2n\pi a^n\left[b^{2n}\left(\mu_1-\mu_2\right)\left(\mu_2-\mu_3\right)+a^{2n}\left(\mu_1+\mu_2\right)\left(\mu_2+\mu_3\right)\right]} \qquad (11)$$

$$B_{n,k}=\frac{2\mu_1 a^{2n}b^{2n}I_k\left(\mu_3-\mu_2\right)}{2n\pi a^n\left[b^{2n}\left(\mu_1-\mu_2\right)\left(\mu_2-\mu_3\right)+a^{2n}\left(\mu_1+\mu_2\right)\left(\mu_2+\mu_3\right)\right]}$$

$$\Delta\alpha_k=\alpha-\alpha_k$$

$$\vec{B}=B_r\vec{a}_r+B_t\vec{a}_t=-\mu_0\vec{\nabla}\Omega\rightarrow\begin{cases}B_r=-\mu_0\dfrac{\partial\Omega}{\partial r}\\ B_t=-\mu_0\dfrac{1}{r}\dfrac{\partial\Omega}{\partial\alpha}\end{cases} \qquad (12)$$

Due to existence of some terms such as r^n, a^n , a^{2n} , b^n, b^{2n} in Hague's solution while n can be reach to infinite number, it can be concluded that the average radius of annular domain in ψ-plane should be 1 meter, $\begin{cases}b<1\\ b\cong 1\end{cases}$, and $\begin{cases}a>1\\ a\cong 1\end{cases}$.

Figure 9

Figure 10

Figure 11

Figure 9 shows the radial component of air-gap flux density under the condition of $I_i=1(A)$. The mutual air-gap permeance obtained through proposed technique and classic method (by Stovic) are compared in Figure 10. As shown, the mutual air-gap permeance is over-estimated by classic method about 22 percent. The air-gap flux tubes are assumed in radial direction by classic method in the overlap region of i^{th} and j^{th} elements. However, this assumption is not acceptable for large air-gap cases. For this reason, the peak value of mutual air-gap permeance calculated by proposed technique is less than the classic method. On the other hand, the expansion and concentration of air-gap flux tubes has been better modeled by proposed technique, as shown in Figure 10.

3. Analysis of MEC model

For the analyzed VREH, the electric resistance (R) and leakage inductance of coil is about 30 (Ω) and 10 (mH), respectively. In general, the coil can be loaded with a resistive load (R_L).

For every wheel position, the non-linear equation system of MEC model including magnetic and electric equations are written as follows:

$$\begin{cases} \dfrac{d\lambda}{dt} = R_L \times I \\ \left[A(u,i)\right]_{(N+1)*(N+1)} \times \begin{bmatrix} [U]_{N*1} \\ I \end{bmatrix}_{(N+1)*1} = \begin{bmatrix} [F]_{N*1} \\ \lambda \end{bmatrix}_{(N+1)*1} \end{cases} \tag{13}$$

where N is the number of nodes in permeance network, $[A(u,i)]_{(N+1)*(N+1)}$ is the permeance matrix, $[U]_{N\times 1}$ is the scalar magnetic potential matrix of nodes, I is the current of coil, $[F]_{N\times 1}$ is the matrix of MMF sources due to PMs, and λ is the flux-linkage of coil.

The Newton-Raphson algorithm is used to solve the non-linear equation system (13) as follows [28]:

$$g(u,i) = \left[A(u,i)\right]_{(N+1)*(N+1)} \times \begin{bmatrix} [U]_{N*1} \\ I \end{bmatrix}_{(N+1)*1} - \begin{bmatrix} [F]_{N*1} \\ \lambda \end{bmatrix}_{(N+1)*1} = [0]_{(N+1)*1}$$

$$\left[J^k\right]_{(N+1)*(N+1)} \times \begin{bmatrix} \Delta u^k \\ \Delta i^k \end{bmatrix}_{(N+1)*1} = \left[-g\left(u^k, i^k\right)\right]_{(N+1)*1} \tag{14}$$

$$\begin{cases} \left[\Delta u^k\right]_{N*1} = \left[U^{k+1}\right]_{N*1} - \left[U^k\right]_{N*1} \\ \Delta i^k = I^{k+1} - I^k \end{cases}$$

where $[J^k]_{(N+1)\times(N+1)}$ is the Jacobian matrix of non-linear system at kth iteration, and $\begin{bmatrix} \Delta u^k \\ \Delta i^k \end{bmatrix}_{(N+1)*1}$ is the incremental vector at k^{th} iteration.

After obtaining the scalar magnetic potential (U) for every rotor position, the electromagnetic torque (T_e) can be calculated as follows:

$$T_e(\theta_r) = 0.5 \times \sum_{i=1}^{n_m} \sum_{j=1}^{n_w} \frac{dG_{i,j}(\theta_r)}{d\theta_r} \left[U_m(i) - U_w(j)\right]^2 \tag{15}$$

where n_m and n_w are the number of elements on the surface and on the both sides of air-gap.

As shown in Figure 11, the flux-linkage with coil can be also calculated as follows:

$$\lambda(\theta_r) = N_c \times \left[P_{i_1-i_2} \left(u_{i_1} - u_{i_2} \right) + P_{j_1-j_2} \left(u_{j_1} - u_{j_2} \right) + P_{k_1-k_2} \left(u_{k_1} - u_{k_2} \right) \right] \quad (16)$$

where N_c is the number of turn of coil, $P_{i_1-i_2}$ is the radial permeance between nodes i_1 and i_2, $P_{j_1-j_2}$ is the radial permeance between nodes j_1 and j_2, and $P_{k_1-k_2}$ is the radial permeance between nodes k_1 and k_2. u_{i_1}, u_{i_2}, u_{j_1}, u_{j_2}, u_{k_1}, and u_{k_2} are the scalar magnetic potential in relevant nodes.

Figure 12

Under no-load condition, Figures 12a-b and Figures 13a-b show the wave-forms of flux-linkage and induced voltage in coil obtained through classic MEC, proposed MEC, and FEM while considering the rotation speed of 250 rpm for toothed wheel, and also the linear and non-linear magnetization characteristic for toothed wheel and m-shaped pole-piece.

Table 2

The DC component and main harmonic component of flux-linkage results obtained through different techniques are compared in Table 2. As shown, the effect of magnetic saturation on the reduction of flux-linkage is less than 2 percent, the flux-linkage is over-estimated by classic technique, and there is also a good agreement between the results obtained through proposed MEC and FEM.

Figure 13

Under the loading condition of coil with $R_L=30\ (\Omega)$ and the rotation of toothed wheel with the speed of 250 (rpm), Figures 14-15 show the results of coil current and electromagnetic torque obtained through three techniques while considering the non-linear characteristic of core. As shown, there is a good agreement between the results of proposed MEC model and FEM.

Figure 14

Figure 15

4. Conclusion

As expected, the conventional MEC model cannot consider the real paths of air-gap flux tubes in overlapping and non-overlapping regions of elements on both sides of air-gap. In real, the flux-linkage and induced voltage in coil are over-estimated by conventional MEC model even considering the large number of elements in MEC model. For this reason, an accurate MEC model was presented in this paper for modeling and analysis of large air-gap electromagnetic

devices such as VREHs. To this end, CMs were used to calculate the mutual air-gap permeances between elements while considering the real paths of flux tubes in all region inside the air-gap. The proposed technique can also consider the fringing of air-gap flux tubes especially in non-overlapping region. According to the results obtained through proposed technique, it can be concluded that the length of air-gap flux tubes in overlapping regions can be larger than the length of radial air-gap flux tubes, particularly in the case of VREHs and other electromagnetic devices with large air-gap.

5. References

[1]. Kishore, R. A., Singh, D., Sriramdas, R., and et al., Sanghadasa, M., and Priya, S., "Linear thermomagnetic energy harvester for low-grade thermal energy harvesting", J APPL PHYS, **127**(4), (2020). DOI: 10.1063/1.5124312.

[2]. Fan, K., Cai, M., Wang, F., and et al., "A string-suspended and driven rotor for efficient ultra-low frequency mechanical energy harvesting", ENERG CONVERS MANAGE, **198**, (2019). DOI: 10.1016/j.enconman.2019.111820.

[3]. Farhat, M., Barambones, O., and Sbita, L., "A new maximum power point method based on a sliding mode approach for solar energy harvesting", APPL ENERG, **185**, pp. 1185-1198, (2017).

[4]. Yang, K., Su, K., Wang, J., and et al., "Piezoelectric wind energy harvesting subjected to the conjunction of vortex-induced vibration and galloping: comprehensive parametric study and optimization", Smart Mater. Struct., **29**(7), (2020). DOI: 10.1088/1361-665X/ab870e.

[5]. Liu, X., Qiu, J., Chen, H., and et al., "Design and optimization of an electromagnetic vibration energy harvester using dual halbach arrays", IEEE T MAGN, **51**(11), (2015). DOI:10.1109/TMAG.2015.2437892.

[6]. Zhang, L. B., Dai, H. L., Yang, Y. W., and et al., "Design of high-efficiency electromagnetic energy harvester based on a rolling magnet", ENERG CONVERS MANAGE, **185**, pp. 202-210, (2019). DOI: 10.1016/j.enconman.2019.01.089.

[7]. Zhang, Y., Wang, T., Luo, A., and et al., "Micro electrostatic energy harvester with both broad bandwidth and high normalized power density", APPL ENERG, **212**, pp. 362-371, (2018). DOI: 10.1016/j.apenergy.2017.12.053.

[8]. Liu, H., Hou, C., Lin, J., and et al., "A non-resonant rotational electromagnetic energy harvester for low-frequency and irregular human motion", Appl. Phys. Lett., **113**(20), (2018). DOI: 10.1063/1.5053945.

[9]. Zhang, Y., Zhu, H., Xu, Y., and et al., "Theoretical modeling and experimental verification of rotational variable reluctance energy harvesters", ENERG CONVERS MANAGE, **233**, (2021). DOI: 10.1016/j.enconman.2021.113906.

[10]. Zhang, Y., Cao, J., Liao, W., and et al., "Theoretical modeling and experimental verifcation of circular Halbach electromagnetic energy harvesters for performance enhancement", Smart Mater. Struct., **27**(9), (2018). DOI: 10.1088/1361-665X/aad710.

[11]. Zhang, Y., Cao, J., Zhu, H., and et al., "Design, modeling and experimental verifcation of circular Halbach electromagnetic energy harvesting from bearing motion", ENERG CONVERS MANAGE, **180**, pp. 811–821, (2019). DOI: 10.1016/j.enconman.2018.11.037.

[12]. Kroener, M., Ravindran, S.K.T., and Woias, P., "Variable reluctance harvester for applications in railroad monitoring", J. Phys. Conf. Ser., **476**, (2013). DOI: 10.1088/1742-6596/476/1/012091.

[13]. Parthasarathy, D., Enoksson, P., and Johansson, R., "Prototype energy harvesting wheel speed sensor for anti-lock braking", Int. Conf. ROSE, (2012). DOI: 10.1109/ROSE.2012.6402607.

[14]. Xu, Y., Bader, S., and Oelmann, B., "A survey on variable reluctance energy harvesters in low-speed rotating applications", IEEE SENS J, **18**(8), pp. 3426-3435, (2018).

[15]. Paul, S., and Chang, J., "Design of novel electromagnetic energy harvester to power a deicing robot and monitoring sensors for transmission lines", ENERG CONVERS MANAGE, **197**, (2019). DOI: 10.1016/j.enconman.2019.111868.

[16]. Cao, Z., Huang, Y., Guo, B., and et al., "A novel hybrid analytical model of active magnetic bearing considering rotor eccentricity and local saturation effect", IEEE T IND ELECTRON, **69**(7), pp. 7151-7160, (2022).

[17]. Ghods, M., and Gorginpour, H., "Equivalent magnetic network modeling of dual-winding outer-rotor vernier permanent magnet machine considering pentagonal meshing in the air-gap", IEEE T IND ELECTRON, **69**(12), pp. 12587-12599, (2022).

[18]. Ding, W., Liang, D., and Tang, R., "A fast nonlinear variable structure equivalent magnetic circuit modeling for dual-channel switched reluctance machine", ENERG CONVERS MANAGE, **52**(1), pp. 308-320, (2011).

[19]. Xu, M., Liu, G., Chen, Q., and et al., "Torque calculation of stator modular PMa-SynRM with asymmetric design for electric vehicles", IEEE T Transport. Electrific., **7**(1), pp. 202-213, (2021).

[20]. Lee, J., Lee, J., and Kim, K., "Design of a WFSM for an electric vehicle based on a nonlinear magnetic equivalent circuit", IEEE T APPL SUPERCON, **28**(3), (2018). DOI: 10.1109/TASC.2018.2807438

[21]. Ostovic, V., "Dynamics of saturated electric machines", Springer-Verlag, (1989).

[22]. Rezaee-Alam, F., Nazari Marashi, A., Dehafarin, A., and et al., "Analytical modelling of one cage rotor induction motor for electric submersible pumps", IET ELECTR POWER APP, **16**(11), pp. 1273-1285, (2022).

[23]. Naderi, P., "Modified magnetic-equivalent-circuit approach for various faults studying in saturable double-cage-induction machines", IET ELECTR POWER APP, **11**(7), pp. 1224-1234, (2017).

[24]. Naderi, P., "Inter-turn short-circuit fault detection in saturable squirrel-cage induction motor using magnetic equivalent circuit model", COMPEL, **35**(1), pp. 245-269, (2016).

[25]. Rezaee-Alam, F., Rezaeealam, B., and Naeini, V., "An improved winding function theory for accurate modeling of small and large air-gap electric machines", IEEE T MAG 2021, **57**(5), (2021). DOI: 10.1109/TMAG.2021.3064402.

[26]. Hague, B., "Electromagnetic Problems in Electrical Engineering". London, U.K.: Oxford Univ. Press, (1929).

[27]. O'Connell, T. C. and Krein, P. T., "A Schwarz-Christoffel-based analytical method for electric machine field analysis", IEEE T ENERGY CONVER, 24(3), pp. 565-577, (2009).

[28]. Asghari, B., "Geometrical permeance network based real-time nonlinear induction machine model", PhD Thesis, University of Alberta, (2011).

Farhad Rezaee-Alam received the B.S. degree from Shahid Chamran University of Ahwaz in 2007, the M.S. and Ph.D. degrees from Khajeh Nasir University of Technology in 2010 and 2015, respectively, all in electrical engineering. He is currently an assistant professor in the

department of electrical engineering, Lorestan University, Iran. His research interests include design and modeling of electric machines.

E-mail: rezaee.fa@lu.ac.ir

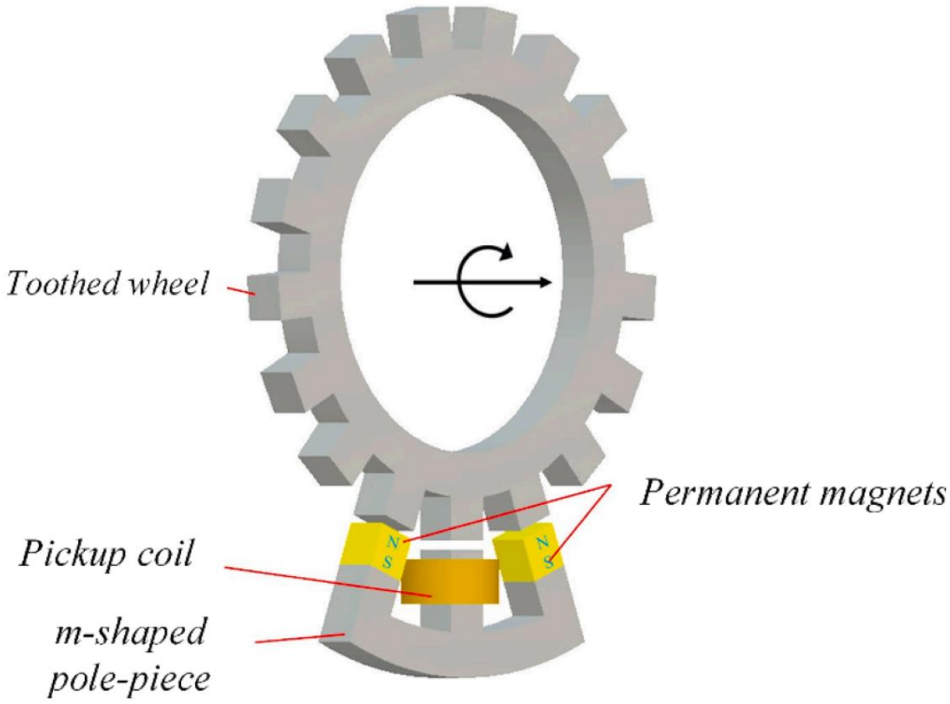

Figure 1

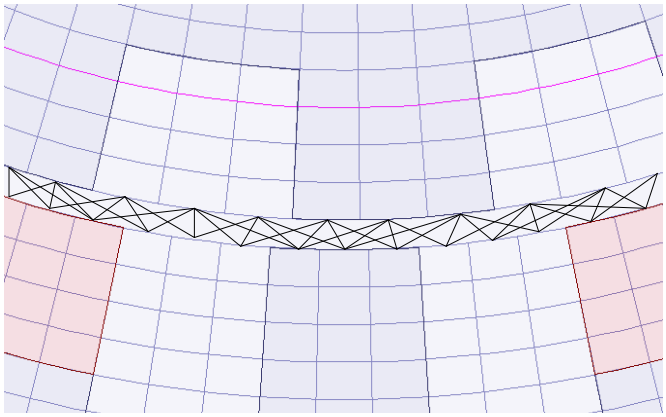

(a)

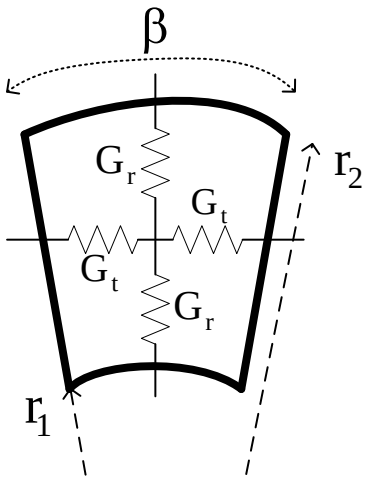

(b)

Figure 2

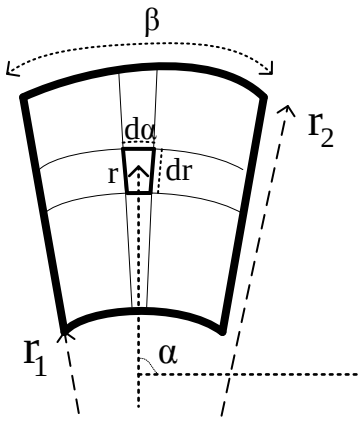

Figure 3

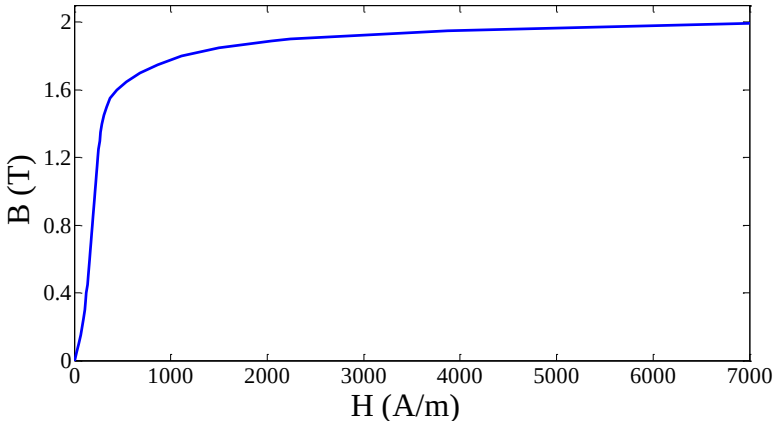

Figure 4

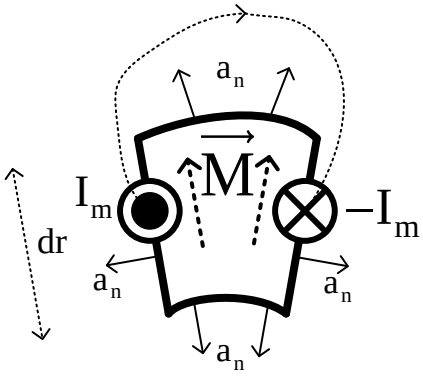

Figure 5

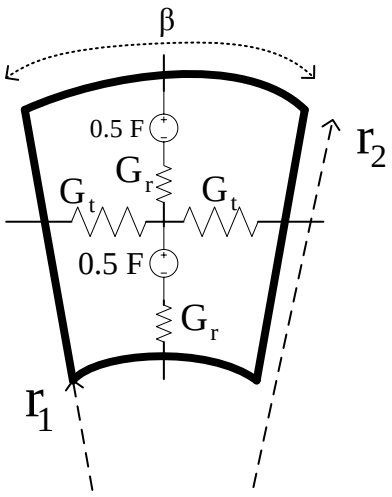

Figure 6

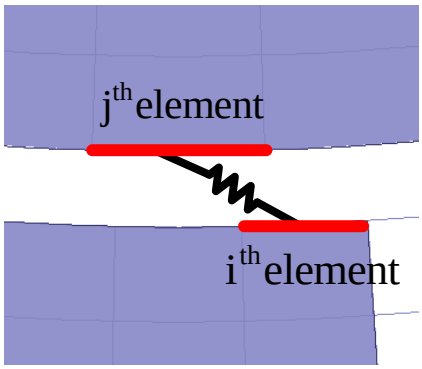

(a)

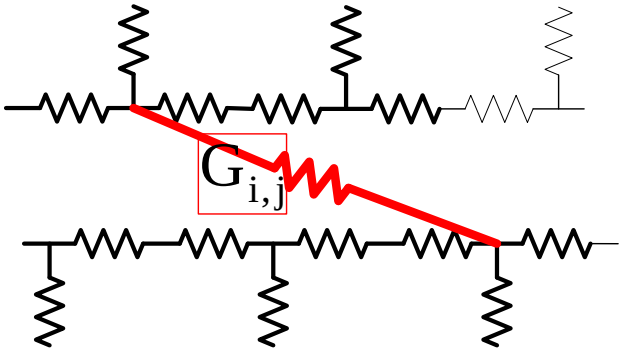

(b)

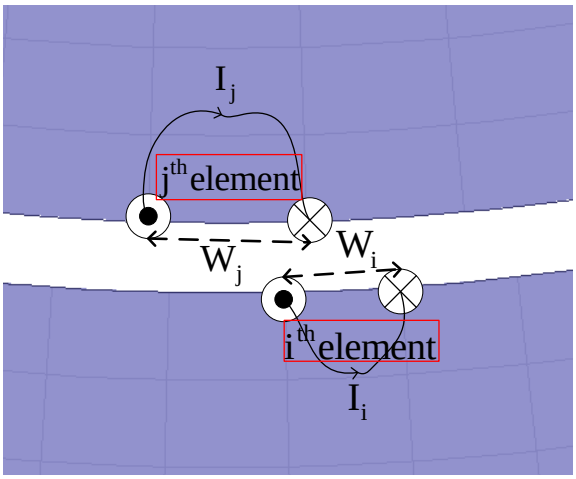

(c)

Figure 7

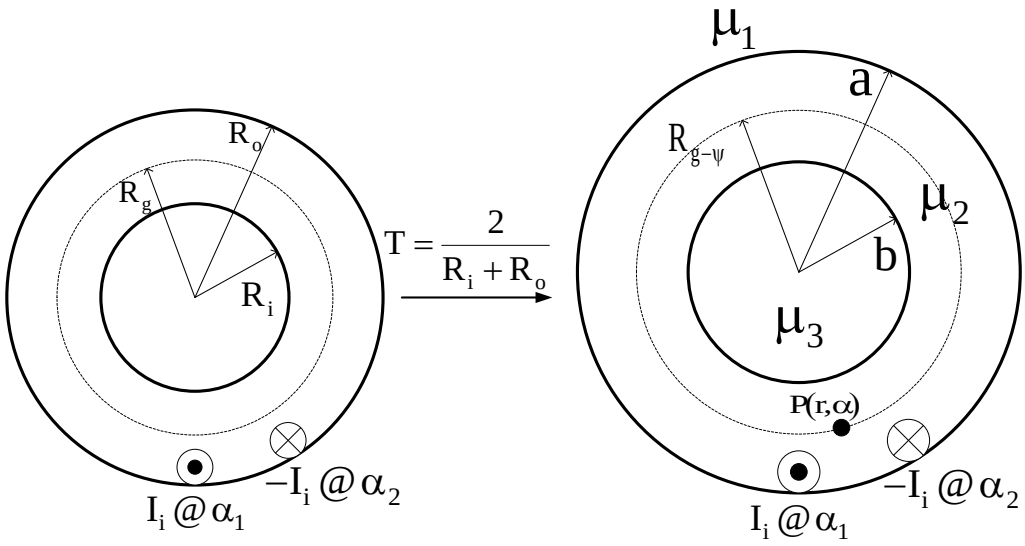

Figure 8

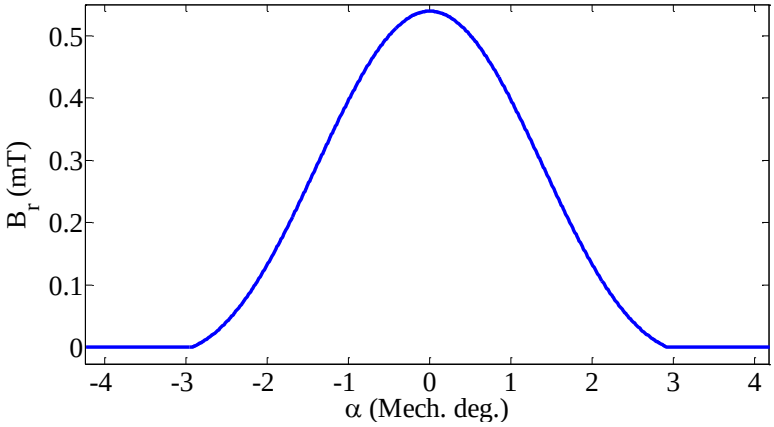

Figure 9

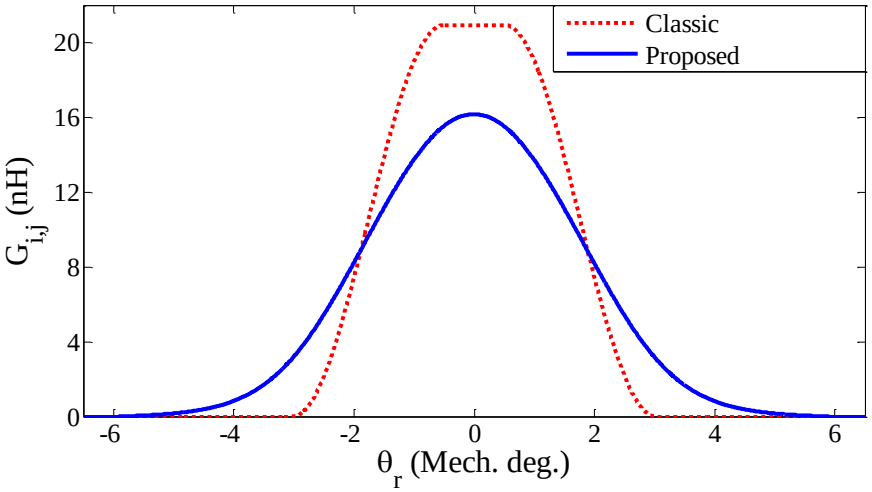

Figure 10

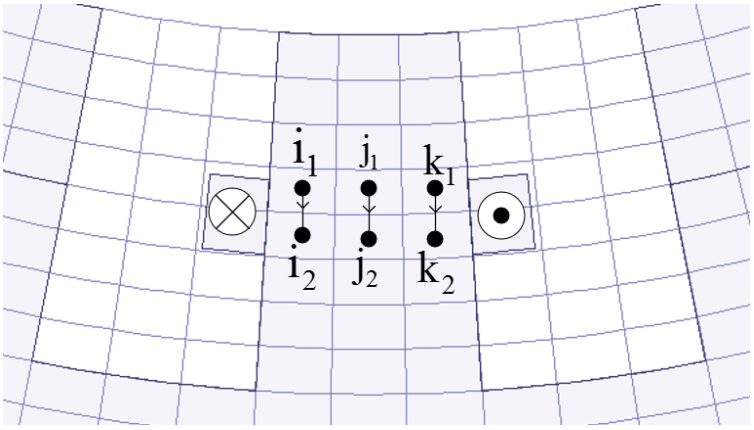

Figure 11

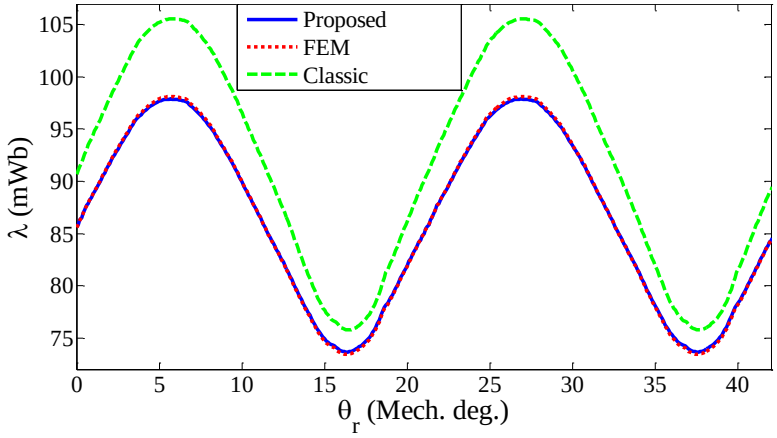

(a)

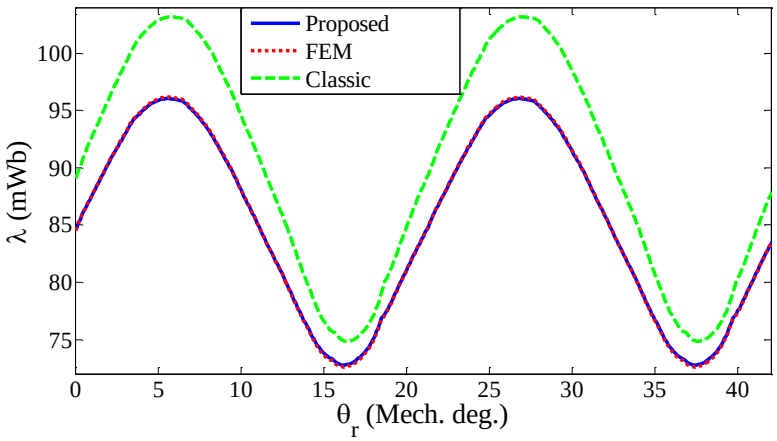

(b)

Figure 12

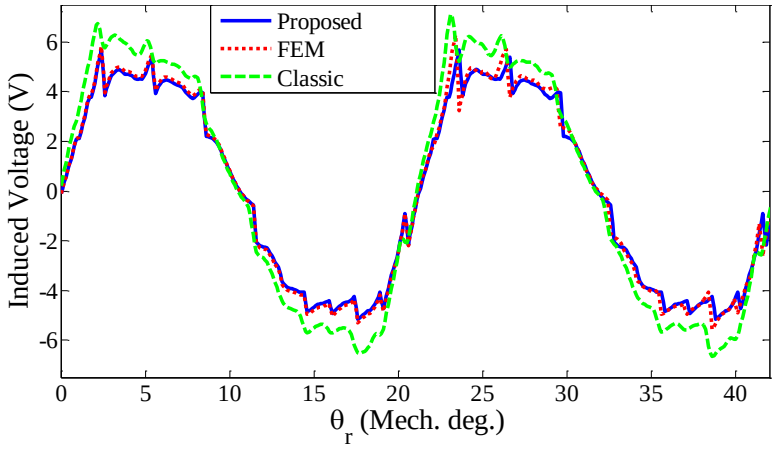

(a)

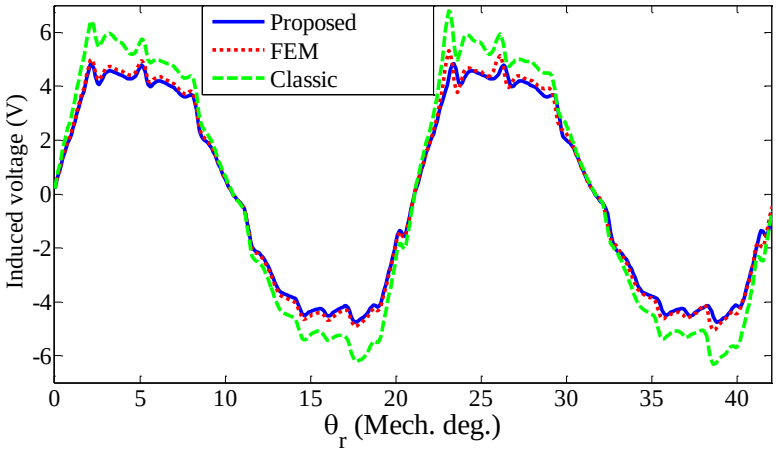

(b)

Figure 13

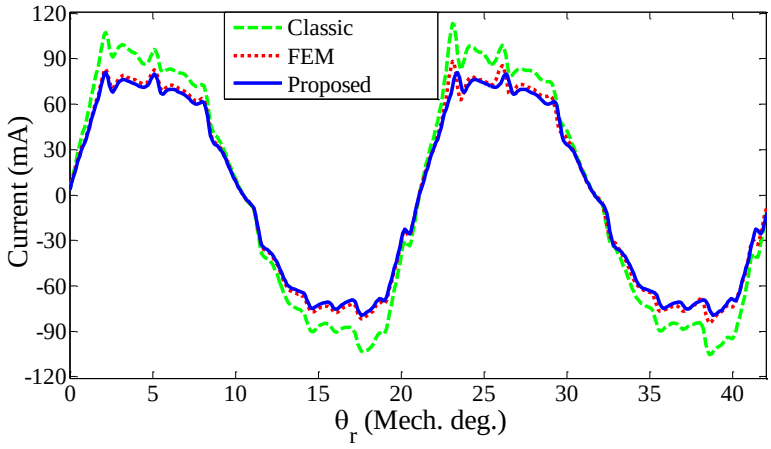

Figure 14

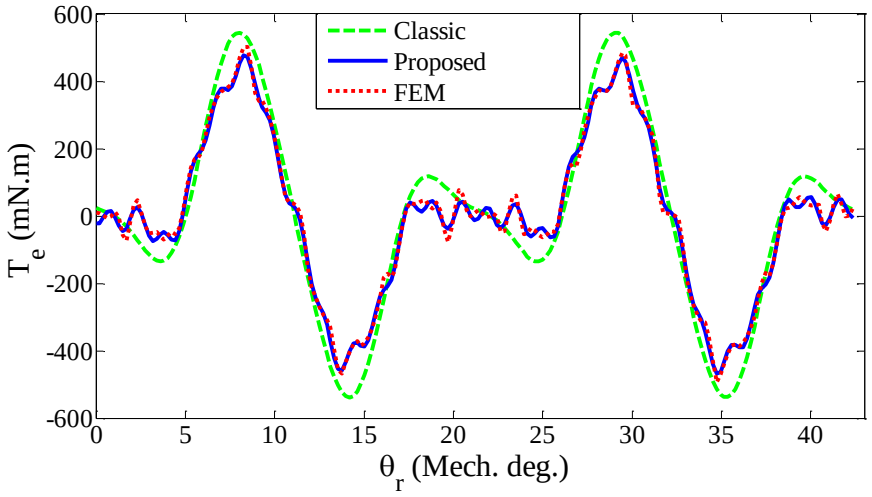
Classic
Proposed
FEM
600
400
200
0
-200
-400
-600
0
5
10
15
20
25
30
35
40
T_e (mN.m)
θ_r (Mech. deg.)

Figure 15

Table 1

Parameter	Value
Size of PMs	10 mm× 10 mm× 10 mm
Remanence of PMs	1.23 T
Magnetic coercivity	890 kA/m
Coil turns	800 turns
Diameter of wire	0.15 mm
Number of teeth	17
Tooth width (wheel)	10 mm
Tooth thickness (wheel)	10 mm
Tooth height (wheel)	9.68 mm
Tooth width (pole-piece)	10 mm
Tooth thickness (pole-piece)	10 mm

Table 2

		DC component	Main component
Linear Model	Classic method	91.8 mWb	14.3 mWb
	Proposed method	86.46 mWb	11.7 mWb
	FEM	86.5 mWb	11.9 mWb
Non-Linear Model	Classic method	90.1 mWb	13.6 mWb
	Proposed method	85.05 mWb	11.2 mWb
	FEM	85.1 mWb	11.4 mWb